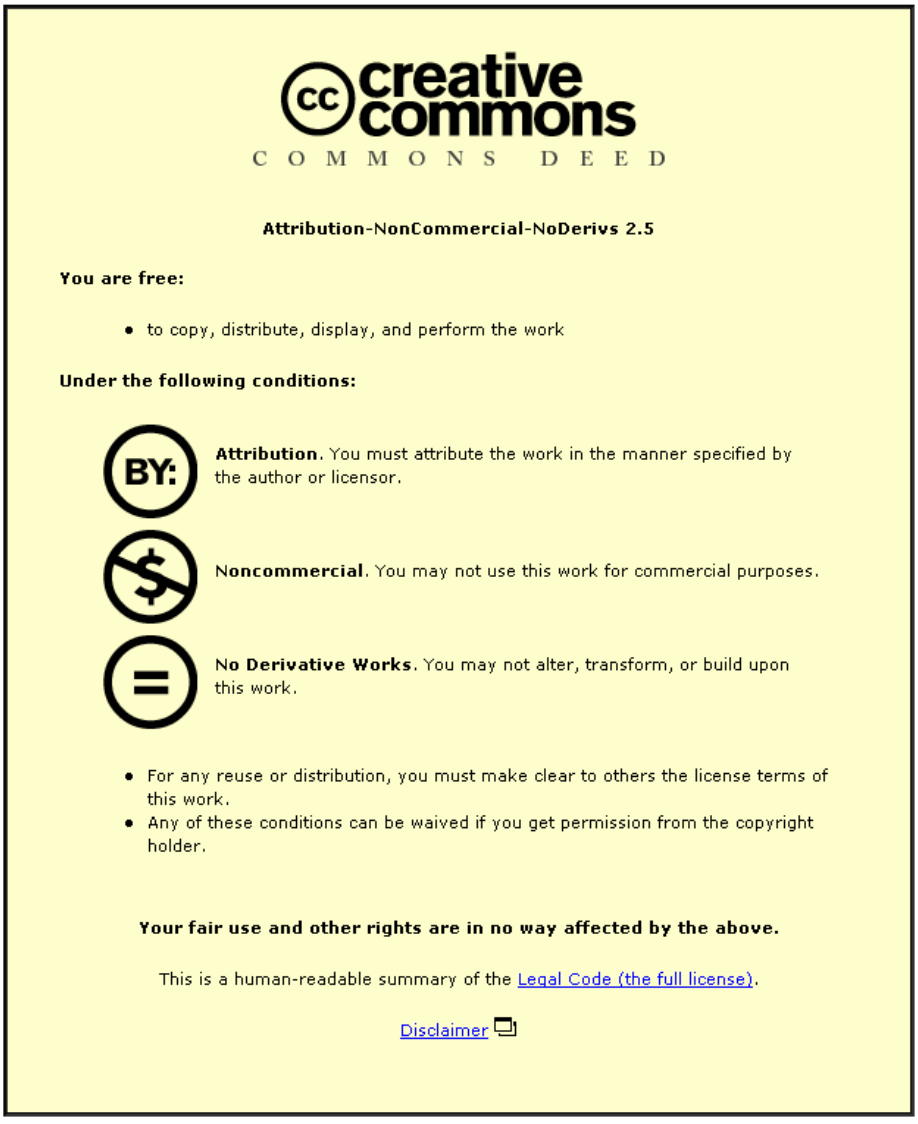

creative commons

COMMONS DEED

Attribution-NonCommercial-NoDerivs 2.5

You are free:

- to copy, distribute, display, and perform the work

Under the following conditions:

BY: **Attribution**. You must attribute the work in the manner specified by the author or licensor.

Noncommercial. You may not use this work for commercial purposes.

No Derivative Works. You may not alter, transform, or build upon this work.

- For any reuse or distribution, you must make clear to others the license terms of this work.
- Any of these conditions can be waived if you get permission from the copyright holder.

Your fair use and other rights are in no way affected by the above.

This is a human-readable summary of the Legal Code (the full license).

Disclaimer

Nonlinear disintegration of the internal tide

Karl R. Helfrich[1] and Roger H. J. Grimshaw[2]

[1] *Department of Physical Oceanography*

Woods Hole Oceanographic Institution

Woods Hole, MA 02543 USA

[2] *Department of Mathematics*

Loughborough University

Loughborough, England

April 2, 2007

Abstract

The disintegration of a first-mode internal tide into shorter solitary-like waves is considered. Because observations frequently show both tides and waves with amplitudes beyond the restrictions of weakly nonlinear theory, the evolution is studied using a fully-nonlinear, weakly nonhydrostatic two-layer theory that included the effects of rotation. In the hydrostatic limit, the governing equations have periodic, nonlinear inertia-gravity solutions that are explored as models of the nonlinear internal tide. These are shown to be robust to weak nonhydrostatic effects. Numerical solutions show that the disintegration of an initially sinusoidal, linear internal tide is closely linked to the presence of these periodic waves. The initial tide steepens due to nonlinearity and sheds energy into short solitary waves. The disintegration is halted as the longwave part of the solution settles onto a state close to one of the nonlinear, hydrostatic solutions, with the short solitary waves superimposed. The degree of disintegration depends upon the initial amplitude of the tide and the properties of the underlying nonlinear solutions, which, depending on stratification and tidal frequency, exist only for a finite range of amplitudes (or energies). There is a lower threshold below which no short solitary waves are produced. However, for initial amplitudes above another threshold, given approximately by the energy of the limiting nonlinear inertia-gravity wave, most of the initial tidal energy goes into solitary waves. Recent observations of large amplitude solitary waves in the South China Sea are discussed in the context of these model results.

1. Introduction

The generation of long internal solitary waves from barotropic tidal flow over localized topography has received much attention over the last few decades due to the ubiquity of these waves in coastal seas and over continental shelves. The usual description involves a downstream lee wave that is released from the topography as the tide turns (e.g. Maxworthy, 1979). Nonlinearity leeds to steepening. Breaking is prevented by nonhydrostatic dispersion and the balance between nonlinearity and dispersion results in the generation of a rank-ordered

packet of solitary waves. Other possible mechanisms include upstream blocking instead of lee wave formation (Lee and Beardsley, 1974), transcritical generation (Grimshaw and Smyth, 1986; Melville and Helfrich, 1987), and the scattering of an internal tide beam at the surface mixed layer (Gerkema, 2001). Which occurs depends on the details of the barotropic flow, stratification, and topography. However, the lee wave release, or more generally the radiation of a low-mode internal tide, that subsequently steepens and disintegrates appears to be the most common mechanism.

A timescale for the emergence of the lead solitary wave from a localized disturbance has been developed by Hammack and Segur (1978) for single layer flows (see Helfrich and Melville (2006) for the two-layer extension) based on weakly-nonlinear Korteweg-de Vries (KdV) theory. The emergence timescale depends on the initial amplitude and lengthscale of the disturbance. Provided that the lengthscale is short compared to the internal deformation radius and that the amplitude is not too large, this estimate should be valid. However, when the initial disturbance lengthscale is comparable to the internal deformation radius, as is the case when the disturbance in a radiating internal tide, or if the emergence timescale is comparable to the local inertial period, the neglected effects of rotation will be important.

Individual solitary waves, because they are short compared to the deformation radius, are typically considered to be unaffected by rotation. However, even weak rotation eliminates permanent form solitary wave solutions in KdV-type theories (Leonov, 1981). An initial solitary wave will decay by radiation damping due to resonance with long inertia-gravity (Poincaré) waves (Melville et al., 1989; Grimshaw et al., 1998a,b). The damping can be significant if the solitary wave propagates for time comparable to the local inertia period. Continued propagation may result in the steepening of the inertia-gravity wave to produce a secondary, growing solitary-like wave behind the original one and the formation of "quasi-cnoidal" wave packets (Helfrich, 2007a).

One the other hand, the propagation of an internal tide, from which the solitary waves may emerge, is fundamentally affected by rotation at all times. The role of rotation in the

disintegration an internal tide into weakly nonlinear solitary waves has been considered by Gerkema and Zimmerman (1995), Gerkema (1996), Holloway et al. (1999), and New and Estaban (1999). The first two are the most relevant. They undertook numerical studies based on the weakly nonlinear Boussinesq equations with rotation (bidirectional propagation versions of KdV). The numerical results showed that unless the barotropic tidal flow over the topography produced an initial disturbance with sufficient nonlinearity, the disintegration of the internal tide into higher frequency solitary waves was inhibited. The radiated internal tide remained a coherent long tide. They argued that the coherence was due to the presence of long, weakly-nonlinear periodic inertia-gravity wave solutions to the hydrostatic limit of the model. In contrast to solitary waves, which require a balance between nonlinearity and nonhydrostatic dispersion, the periodic inertia-gravity waves arise from the balance of nonlinearity with rotational dispersion. These nonlinear solutions were first found by Ostrovsky (1978) in a study of the rotationally modified KdV equation. These hydrostatic solutions exist only up to a limiting amplitude, beyond which the rotational dispersion is not able to balance the nonlinearity. This led Gerkema (1996) to propose a threshold argument for the disintegration of the tide based on the nonlinearity of the initial tide (given by a measure of the forcing strength related to the barotropic tide, stratification, and topographic slope). If the amplitude (i.e. nonlinearity) was above the limiting amplitude, the long tide solutions were not generated. Instead, the tide would disintegrate with most of the initial tide evolving rapidly into shorter solitary waves. If less than the threshold, then disintegration was strongly inhibited. They also noted that for a given forcing amplitude and frequency, increasing rotation (i.e. latitude) inhibited the disintegration of the internal tide. New and Estaban (1999) noted that increasing the tidal frequency had the same effect as a decrease in latitude.

The goal of this paper is to explore further the role of rotation in the evolution of the low-mode nonlinear internal tide and the production of shorter, nonhydrostatic solitary waves. This process can be viewed as a competition between high-frequency nonhydrostatic dispersion and low-frequency rotational to balance the nonlinear steepening of the propagating tide. However, numerous recent observations show that both the tides and solitary waves are in

many places quite large (e.g. Stanton and Ostrovsky, 1998; Ramp et al., 2005) so that a weakly nonlinear theory may be inadequate. Thus the restriction to weak nonlinearity will be eliminated, while retaining the assumption of weak nonhydrostatic effects. The inclusion of full nonlinearity has the added benefit that the properties of the hydrostatic, nonlinear inertia-gravity waves that appear to play a substantial role the disintegration of the internal tide can be significantly different when compared to the weakly nonlinear models. Furthermore, no assumption about the strength of the rotation effects, as is required by unidirectional KdV-type theories, is necessary.

The paper is organized as follows. Section 2 introduces the mathematical model for a rotating, two-layer flows with $O(1)$ nonlinearity and weak nonhydrostatic effects. Properties of the solitary wave solutions to these equations in the absence of rotation are given. The nonlinear, hydrostatic inertial-gravity waves solutions are then found. This part builds upon work by Shrira (1986) for a single layer and Plougonven and Zeitlin (2003) for a two-layer flow. In Section 3 numerical solutions to the full equations are explored for sinusoidal linear inertia-gravity wave (e.g. tide) initial conditions. In Section 4 the results are summarized and then discussed in the context of recent observations of large amplitude internal tides and solitary waves in the South China Sea.

2. The Model

The situation under consideration is an inviscid, two-layer fluid with layer depths h_i and velocity vectors $\mathbf{u}_i$. Here $i = 1$ and 2 refer to the upper and lower layers, respectively. The layer densities are ρ_1 and $\rho_2 = \rho_1 + \Delta\rho$. The system is rotating about the z-axis with constant Coriolis frequency f (> 0). The gravitational acceleration g is directed in the negative z-direction. In the absence of motion $h_1 = h_0$ and $h_2 = H - h_0$, where H is the total depth. The bottom is flat and the upper surface is rigid.

The propagation of nonlinear interfacial waves in this system will be studied in the limit of fully nonlinear, $\alpha = a/h_s = O(1)$, and weakly nonhydrostatic long waves, $\beta = (h_s/l)^2 \ll$

1. Here α and β are the usual parameters describing nonlinear and nonhydrostatic effects, respectively. h_s is a depth scale, and a and l are, respectively, scales for the amplitude and length of the waves. KdV theory requires $\beta = O(\alpha) \ll 1$. No restriction is placed on the relative magnitude of the rotational effects. In the absence of rotation a set of equations for fully nonlinear, weakly nonhydrostatic interfacial waves has been developed Miyata (1987) and Choi and Camassa (1999) (denoted here as the MCC equations for brevity). The extension of the MCC theory to include rotation is discussed in (Helfrich, 2007a), so only the resulting equations are given below.

The waves will be taken to propagate in the x-direction. With rotation, motion in the transverse y-direction will occur; however, the flow will be taken to be independent of y so that $\partial/\partial y = 0$. The continuity and vertically averaged x and y momentum equations for each layer, including the Coriolis terms, are respectively

$$h_{it} + [h_i \bar{u}_i]_x = 0 \tag{1}$$

$$\bar{u}_{it} + \bar{u}_i \bar{u}_{ix} - f\bar{v}_i = -g\eta_x + \frac{1}{\rho_i} P_x + D_i + O(\beta^2) \tag{2}$$

$$\bar{v}_{it} + \bar{u}_i \bar{v}_{ix} + f\bar{u}_i = O(\beta^2). \tag{3}$$

Here the overbar indicates a vertical average over a layer, u_i and v_i are, respectively, the velocities in the x and y-directions, $\eta(x,t) = h_0 - h_1$ is the interface displacement, and $P(x,t)$ is the pressure at the interface. The subscripts t and x indicate differentiation. The $O(\beta)$ nonhydrostatic effects are given by (Choi and Camassa, 1999)

$$D_i = h_i^{-1} \left[\tfrac{1}{3} h_i^2 \left(\bar{u}_{ixt} + \bar{u}_i \bar{u}_{ixx} - (\bar{u}_{ix})^2 \right) \right]_x . \tag{4}$$

In the weakly nonlinear limit ($\alpha \ll 1$)

$$D_2 - D_1 = \tfrac{1}{3}(h_0 - h_0^2) s_{xxt} + O(\alpha\beta). \tag{5}$$

Equations (1), (2), and (3) are nondimensionalized using $\sqrt{g'H}$, H, l, and $l/\sqrt{g'H}$ for $(\bar{u}_i,\ \bar{v}_i)$, h_i, x, and t, respectively. The reduced gravity $g' = g\Delta\rho/\rho_1$. The equations are simplified by eliminating P_x between (2) and (3). The Boussinesq approximation $\Delta\rho/\rho_1 \ll 1$

is also employed since it is reasonable in the oceanic context and consistent with the rigid-lid assumption. The nondimensional, rotating MCC equations (referred to as MCC-f) are

$$h_{1t} + [sh_1(h_1 - 1)]_x = 0 \tag{6}$$

$$s_t + \left[\tfrac{1}{2}s^2(2h_1 - 1) - h_1\right]_x - \gamma v = \beta(D_2 - D_1) \tag{7}$$

$$v_t + svh_{1x} + s(2h_1 - 1)v_x + sV_x + \gamma s = 0 \tag{8}$$

$$V_t + [svh_1(1 - h_1)]_x = 0. \tag{9}$$

Here $s = \bar{u}_2 - \bar{u}_1$ and $v = \bar{v}_2 - \bar{v}_1$. Note that η $(= h_0 - h_1)$ has been eliminated in favor of h_1 and $h_2 = 1 - h_1$. The barotropic transports in the x and y- directions are, respectively,

$$U = \bar{u}_1 h_1 + \bar{u}_2 h_2, \qquad V = \bar{v}_1 h_1 + \bar{v}_2 h_2. \tag{10}$$

With the rigid lid $U = U(t)$ and must be specified. In (6)-(9) it has been set to $U = 0$. The nonhydrostatic terms D_i are given by (4) with $\bar{u}_1 = s(h_1 - 1)$ and $\bar{u}_2 = sh_1$.

The two parameters that appear in (6)-(9) are

$$\gamma = \frac{l}{L_R}, \qquad\qquad \beta = (\frac{H}{l})^2 \tag{11}$$

where the scaling depth h_s is set to H in β. The internal deformation radius $L_R = \sqrt{g'H}/f$. The parameter γ, essentially the inverse of a Rossby number, measures the relative effects of rotation. Unlike most weakly nonlinear theories (e.g. Ostrovsky, 1978; Gerkema, 1996), γ is not restricted to be small. This is particularly important in the present context since the internal tide has $l \approx L_R$ (or $\omega/f = O(1)$, where ω is the frequency).

The MCC-f equations can be manipulated to obtain an energy equation (following Choi and Camassa, 1999; Helfrich, 2007a). The total energy between x_1 and x_2 is

$$E = \int_{x_1}^{x_2} \left[\frac{1}{2}\eta^2 + \sum_{i=1}^{2} \frac{1}{2}\left(h_i(\bar{u}_i^2 + \bar{v}_i^2) + \frac{1}{3}\beta h_i^3 \bar{u}_{ix}^2\right)\right] dx. \tag{12}$$

a. $\gamma = 0$: non-rotating internal solitary waves

With no rotation, $\gamma = 0$, and β finite, (6) and (7) reduce to the (non-rotating) MCC equations. If $v = V = 0$ at $t = 0$, they remain zero from (8) and (9). Solitary waves solutions to (6) and (7) for the form $\eta = \eta(\xi)$, where $\xi = x - ct$, can then be found from (Miyata, 1987; Choi and Camassa, 1999; Miyata, 1985)

$$\left(\frac{d\eta}{d\xi}\right)^2 = \beta^{-1} 3\eta^2 \left[\frac{1 - c^{-2}(h_0 - \eta)(1 - h_0 + \eta)}{h_0^2(1 - h_0 + \eta) + (1 - h_0)^2(h_0 - \eta)}\right], \tag{13}$$

with the shear $s(\xi)$ given by

$$s = \frac{c\eta}{(h_0 - \eta)(1 - h_0 + \eta)}. \tag{14}$$

The solitary wave phase speed

$$c = \pm[(h_0 - \eta_0)(1 - h_0 + \eta_0)]^{1/2} \tag{15}$$

and η_0 is the wave amplitude. For $\eta_0 \to 0$, $c \to \pm c_0$ where

$$c_0 = (h_0 - h_0^2)^{1/2} \tag{16}$$

is the linear two-layer longwave phase speed.

As in weakly nonlinear theory, the solitary waves point into the deeper layer so that $\eta_0 < 0$ (> 0) for $h_0 < 0.5$ (> 0.5). There are no solitary wave solutions for $h_0 = 0.5$. Solitary waves are limited to a maximum amplitude $\eta_{0max} = h_0 - 0.5$ that reaches mid-depth. This limiting wave has infinite wavelength and is a smooth, dissipationless transition between two uniform (conjugate) states. These "thick" solitary waves and conjugate states do not occur in the KdV equation, but do appear when the cubic nonlinearity is included in the KdV-type models (Kakutani and Yamasaki, 1978; Helfrich and Melville, 2006). These MCC solitary waves agree quite well with full nonhydrostatic numerical calculations, laboratory experiments, and oceanic observations (e.g. Choi and Camassa, 1999; Michallet and Barthelemy, 1998; Ostrovsky and Grue, 2003; Camassa et al., 2006).

The MCC equations, unlike their weakly nonlinear counterparts, do not filter out Kelvin-Helmholtz instability (Jo and Choi, 2002). As a consequence, the solitary waves can be

unstable at high wave numbers. Numerical solutions of the MCC equations show that if the grid resolution is too fine, unstable short waves first emerge near the wave crest and ultimately overwhelm the calculations (Jo and Choi, 2002). This instability is enhanced for large amplitude waves, especially as h_0 becomes small (or approaches one). The instability can be controlled by filtering out wavenumbers above the linear stability threshold (W. Choi, pers. comm.).

b. $\beta = 0$: nonlinear internal inertia-gravity (tidal) waves

In the limit $\beta = 0$ with γ finite, (6)-(9) are simply the two-layer shallow-water equations. The absence of nonhydrostatic dispersion eliminates solitary wave solutions. However, periodic, finite-amplitude inertia-gravity wave solutions can be found (Plougonven and Zeitlin, 2003). These solutions are the two-layer extensions of the exact, fully nonlinear single-layer inertia-gravity wave solutions found by Shrira (1986). As in the weakly nonlinear limit, these periodic solutions arise from a balance between nonlinearity and low-frequency rotational dispersion. Here we examine these periodic two-layer solutions. The analysis below follows Plougonven and Zeitlin (2003); however, some new features of the solutions are discussed with an emphasis on their properties as models of the internal tide.

We seek steadily propagating periodic solutions of (6)-(9) the form $h_1(\xi)$, where $\xi = x - ct$, and c is the phase speed. Thus the continuity equation (6) gives, after integration in x and requiring that $s \to 0$ as $h_1 \to h_0$,

$$s = \frac{c(h_0 - h)}{h(1-h)}.$$

Note that for simplicity the subscript 1 has been dropped from h_1 $(= h)$. Using this result in the x-momentum equation (7) (with $\beta = 0$) gives after simplification

$$\frac{dF}{d\xi} = \gamma v, \tag{17}$$

where

$$F(h) = \frac{c^2}{2}\left\{\frac{(1-h_0)^2}{(1-h)^2} - \frac{h_0^2}{h^2}\right\} - h. \tag{18}$$

The shallow water equations, (1)-(3) with $\beta = 0$, conserve the potential vorticity in each layer,

$$q_i = \frac{1 + \gamma \bar{v}_{ix}}{h_i}. \tag{19}$$

This equation has been nondimensionalized as described above so that q_i is scaled by f/H. The requirement that $\partial/\partial y = 0$ has also been used. With the potential vorticity set to the resting value in each layer, $q_1 = h_0^{-1}$ and $q_2 = (1 - h_0)^{-1}$, (19) can be used to find

$$v_x = \gamma \frac{h_0 - h}{h_0 - h_0^2}. \tag{20}$$

These values of the potential vorticity are not arbitrary. The same result is obtained directly from (8) and (9).

Using (20) to eliminate v in (17) gives

$$\frac{d^2F}{d\xi^2} = \gamma^2 \frac{h_0 - h}{h_0 - h_0^2}.$$

Multiplication by F_ξ and integration gives

$$\left(\frac{dh}{d\xi}\right)^2 = \left(\frac{2\gamma^2}{c_0^2}\right) \frac{D - g(h)}{(F')^2}, \tag{21}$$

where D is a constant of integration, $F' = dF/dh$, and

$$g(h) = \frac{1}{2}(h - h_0)^2(c^2\phi(h) - 1), \qquad \phi(h) = \frac{c_0^2 + (h - h_0)^2}{h^2(1 - h)^2}. \tag{22}$$

For periodic waves, continuity requires

$$\int_0^\lambda h d\xi = 0,$$

where λ is the wavelength. This then implies that h oscillates between h_m and h_M, where $0 \le h_m < h_0 < h_M \le 1$. Without loss of generality we will limit discussion of solutions of (21) to $h_0 \le 0.5$. Because of the symmetry inherent in the equations with the Boussinesq approximation, solutions for $h_0 \ge 0.5$ can be obtained by taking h_0 to be the mean depth of the lower layer and h_2 given by the solution $h(\xi)$ of (21). We will refer to the point where

$h = h_m$ as the trough of the wave and h_M as the crest even though for $h_0 < 0.5$ these points correspond to the maximum and minimum interfacial displacement $\eta = h_0 - h$, respectively. Similarly, we will refer to $h_M - h_0$ as the wave amplitude since, as will be shown below, $h_M - h_0 \geq h_0 - h_m$.

The nature of periodic solutions to (21) depends critically on the denominator $F'(h)$. Smooth solutions require that $F'(h) \neq 0$ in $h_m \leq h \leq h_M$. Should $F'(h) = 0$ in this range, then $h_x \to \infty$. We will for the moment suppose that this does not occur. For a smooth, periodic solution $h_x = 0$ at $h = h_m$ and h_M. This sets the constant of integration

$$D = g(h_m) = g(h_M),$$

from which a relation for c can be found using (22),

$$c^2 = \frac{(h_M - h_0)^2 - (h_m - h_0)^2}{(h_M - h_0)^2\phi(h_M) - (h_m - h_0)^2\phi(h_m)}. \tag{23}$$

It follows from (21) that $D - g(h) \geq 0$ for $h_m \leq h \leq h_M$. For smooth solutions $F'(h) > 0$, and since $h_m \leq h_0 \leq h_M$, $F'(h_0) > 0$. From (18), $F'(h_0) = c^2/c_0^2 - 1$, therefore $c^2 > c_0^2$.

If, on the other hand, $F'(h) = 0$, then the first zero of this function sets the upper bound for h_M. As solutions approach this limit, they take on a "corner wave" shape similar to what is found in the weakly-nonlinear theory (Ostrovsky, 1978; Grimshaw et al., 1998b) and the fully nonlinear single-layer model (Shrira, 1986).

Whether this limiting corner wave occurs (for a given h_0) depends on c. From (18)

$$F'(h) = c^2\left[\frac{h_0^2}{h^3} + \frac{(1-h_0)^2}{(1-h)^3}\right] - 1. \tag{24}$$

The minimum of F' occurs at

$$h = \hat{h} = \frac{h_0^{1/2}}{(1-h_0)^{1/2} + h_0^{1/2}},$$

and $F'(\hat{h}) = 0$ for $c = c_*$, where

$$c_* = \left[\frac{(1-h_0)^2}{(1-\hat{h})^3} + \frac{h_0^2}{\hat{h}^3}\right]^{-1/2}. \tag{25}$$

The behavior of $F'(h)$ is illustrated in Figure 1. $F'(\hat{h}) > 0$ (≤ 0) for $c > c_*$ ($\leq c_*$). Thus for $c \leq c_*$ a limiting corner wave occurs with the upper bound on h_M given by the first zero of $F'(h)$.

These two types of waves are illustrated in Figure 2. The upper panel shows the interface $\eta(\xi) = h_0 - h$ over one wavelength for waves with $h_0 = 0.25$ and frequency $\omega = 1.4$ ($= \omega/f$ in dimensional variables), found by numerical integration of (21). The parameter $\gamma = 1$. As the waves amplitude increases the profiles take on a square, or lobate, shape, but remain smooth. The maximum wave for this frequency is $h_M = 0.5504$. The wave profiles are asymmetric with $h_M - h_0 \geq h_0 - h_m$. The corner wave class is illustrated in the lower panel where $\omega = 2$. The crest becomes increasingly peaked until the limiting wave, at $h_M = 0.3061$, is reached. The solution can then be constructed as a sequence of arcs in analogy with the sequence of parabolic arcs found in the weakly-nonlinear theory (Ostrovsky, 1978; Grimshaw et al., 1998b). We discuss below how these families with fixed ω are found.

A convenient way to illustrate the solutions is to consider where h_m-h_M plane, for a given h_0, periodic solutions occur. An example is shown in Figure 3a for $h_0 = 0.25$. Periodic waves can be found everywhere within the indicated lines, which represent different limits of the possible wave speeds c. These boundaries are determined as follows. The limit $c \to \infty$ is found by setting the denominator of (23) to zero. This gives a relation between h_m and h_M that is shown by the lowest curve in Figure 3a and provides a lower bound on h_M given h_m. A portion of the upper bound can be deduced from Figure 1. To find solutions with $h_M \geq \hat{h}$ requires $c \geq c_*$. Thus setting $c = c_*$ in (23) and solving the resulting equation for $h_M(h_m)$ gives the curve extending from $h_M = 1$ to the small solid circle where $h_M = \hat{h}_M = \hat{h}$. The associated value of $h_m = \hat{h}_m$. No solutions with $c < c_*$ and $h_m < \hat{h}_m$ are possible since then the first zero of $F'(h)$ occurs for $h < \hat{h}_M$. So for $h_m \leq \hat{h}_m$ ($h_M \geq \hat{h}_M$) the wave speed $c_* \leq c \leq \infty$.

The c_* curve extends to $h_m = h_0$; however, for $h_m > \hat{h}_m$ this curve no longer defines the upper bound on h_M. In this range the upper bound on the wave speed, c_{lim} ($c_0 \leq c_{lim} \leq c_*$)

is given by the first zero of $F'(h)$ from (24). These zeros give $h_M = h_M(c)$ and (23) gives the corresponding h_m. This curve is indicated by $c = c_{lim}(h_m)$ in Figure 3a. Thus for a fixed $h_m > \hat{h}_m$, the waves approach limiting corner-wave shape as h_M increases.

Figure 3b shows lower right portion of the h_m-h_M plane for $h_0 = 0.25$ with the loci of waves with several values of frequency $\omega = ck$, where $k = 2\pi/\lambda$ is the wavenumber. For $\omega = 2$ (the semi-diurnal tide at 30°) the maximum amplitude wave is a corner wave with $c = 0.5088$ at $(h_m, h_M) = (0.2274, 0.3061)$. For the lower frequency $\omega = 1.4$ (the semi-diurnal tide at 44°) the amplitude is limited by the approach to $c = c_* = 0.5359$ at $(h_m, h_M) = (0.1475, 0.5504)$. Here the waves take on the lobate shape. The division between the cases occurs for $\omega = 1.796$. The waves shown in Figure 2 fall along these two lines. It is interesting that sub-inertial, $\omega < 1$, waves can be found. They are in the lobate class and have large amplitudes. The dashed line shows the solutions with $\lambda = 2.78$, the wavelength of linear waves with $\omega = 1.4$ from the linear inertia-gravity dispersion relation $\omega^2 = \gamma^2 + c_0^2 k^2$ with $\gamma = 1$.

The wavelength is found from the integration of (21)

$$\frac{\lambda}{2} = \int_0^{\lambda/2} d\xi = \frac{c_0}{2^{1/2}\gamma} \int_{h_m}^{h_M} \frac{F'(h)}{[D - g(h)]^{1/2}} dh. \tag{26}$$

The denominator is zero at both limits, so numerical integration employs a Taylor expansion at each end. Waves of a particular frequency or wavelength are found from tabulating the properties of solutions within the allowable h_M range.

The effect of changing h_0 is shown in Figure 4 where the regions of periodic solutions are plotted for several values of h_0. Also shown for each case is the range of solutions with $\omega = 1.4$. As h_0 decreases, the range of solutions with $\omega = 1.4$ decreases and the limiting wave changes from a lobate class to the corner wave. As in Figure 3b, all solutions with $\omega > 1.4$ fall to the right (with smaller amplitudes) of this curve. It is also interesting to note that for $h_0 = 0.5$ the waves are symmetric. They all fall along the line $h_m = h_M$, and are in the lobate class. The maximum amplitude wave with $\omega = 1.4$ is indicated by the square.

Lastly, dispersion curves c versus amplitude $h_M - h_0$ for $\omega = 1.4$ are plotted in Figure 5. The speed is scaled by $c_{0f} = c_0(1 - \omega^{-2})^{-1/2}$, the linear inertia-gravity wave phase speed.

Finite amplitude can either increase or decrease c compared to the linear speed c_{0f}, and the amplitude dispersion does not have to be monotonic.

c. Finite β and γ

When both nonhydrostatic and rotation are present there are no known analytical solutions to the MCC-f equations (6)-(9). Numerical solutions have so far only examined the effect of rotation on the evolution of an initial non-rotating MCC solitary wave from (13) (Helfrich, 2007a). As in earlier weakly-nonlinear studies (Grimshaw et al., 1998a) it was found that the solitary wave decayed by radiation of a longer inertia-gravity wave. On longer time scales, the inertia-gravity wave itself steepened to produce a secondary, growing solitary -like wave. This decay and re-emergence process repeated until a nearly localized wave packet consisting of a long envelop through which a train of faster solitary-like, or quasi-cnoidal, waves propagate.

The situation of an initial condition given by a long, hydrostatic inertia-gravity wave, either a linear sinusoidal wave, or one of the fully nonlinear solutions just described, has not been explored and is the focus of this study. In particular, parameters relevant for the propagation and possible disintegration of an internal tide will be considered.

3. Numerical solutions

To organize the presentation of results the lengthscale l will be set to L_R in (11), giving $\gamma = 1$ and $\beta = (H/L_R)^2 = Hf^2/g'$ in (6)-(9). This choice is arbitrary and it is possible to take $l = H$, giving $\beta = 1$ and $\gamma = H/L_R$. In either case, the sole remaining parameter is H/L_R. Conversion between them amounts to a rescaling of x and t. In the former scaling the long inertia-gravity waves have lengths of $O(1)$ and the nonhydrostatic waves are an order-of-magnitude shorter. Typical mid-latitude values of $H = 100 - 3000$ m (coastal to deep ocean), $f \approx 10^{-4}$ s^{-1}, and $g' \approx 0.01$-0.05 m s^{-2} give $\beta \approx [0.2 - 30] \times 10^{-4}$. Thus, $\beta^{1/2} = H/L_R = [0.5 - 5] \times 10^{-2}$ is representative of oceanic conditions.

a. Methods

The MCC-f equations, (6)-(9), are solved with the numerical method developed by Wei et al. (1995) for a set of wave equations that are closely related to the non-rotating single-layer version of the MCC equations. The method uses centered, fourth-order finite differences for all x derivatives except those in D_i, which are differenced using centered, second- order stencils. Temporal integration is a fourth-order Adams-Bashforth-Moulton predictor-corrector scheme with iteration on the corrector step. Only minor modifications of the scheme are necessary for the MCC-f equations. The scheme was successfully tested by checking solitary wave propagation in the absence of rotation. The solitary wave instability (Jo and Choi, 2002) was found in some cases, and could be controlled by the periodic removal of high wavenumbers (W. Choi, personal communication).

Solutions of the nonhydrostatic MCC-f equations are compared to solutions in the hydrostatic limit $\beta = 0$. In this limit, though, the numerical scheme above fails if wave breaking occurs. Thus for the hydrostatic runs the non-oscillatory-central shock-capturing scheme of Jiang and Tadmor (1998) is used.

The numerical domain is periodic in x. The resolution in x varies from 600 to over 1000 grid points to insure that any short solitary-like waves are properly resolved.

b. Results

The hydrostatic nonlinear inertia-gravity waves (nonlinear tides) are quite robust to weak nonhydrostatic effects. Figure 6a shows the evolution of a large-amplitude nonlinear tide solution of the lobate class for $h_0 = 0.25$ and $\lambda = 2.8$ with $h_m = 0.18$ ($h_M = 0.4229$ and $c = 0.6162$) after eight periods of propagation for $\beta^{1/2} = 0.02$ and 0.04. The only appreciable effect of the nonhydrostatic terms is a weak decrease of the phase speed with increasing β. The wave shapes and amplitudes are essentially unchanged. A similar calculation for an initial wave of the corner class is shown in Figure 6b with $h_0 = 0.1$, $\lambda = 2.024$, $h_m = 0.085$, $h_M = 0.139$, and $c = 0.4513$. This initial wave is quite close to the limiting corner wave at

$h_M = 0.1401$ for these values of h_0, h_m, and λ. Again, the weak nonhydrostatic dispersion leads to a decrease in waves speed that is slightly more pronounced than the previous example. The wave amplitude is affected with increasing β leading to a smoothing of the wave crest and a small reduction of the amplitude. The corner shape of the wave induces the enhanced sensitivity to nonhydrostatic effects. Still, the overall wave shape is stable. The balance between nonlinearity and rotational dispersion that gives the nonlinear inertia-gravity wave solutions is not broken by weak nonhydrostatic effects. These two examples are representative of other cases with similarly small, oceanographically realistic values of β.

Because of their stability to weak nonhydrostatic effects, the fully nonlinear hydrostatic inertia-gravity waves likely play an important role in the evolution of more general initial conditions as suggested by the weakly nonlinear studies of Gerkema and Zimmerman (1995) and Gerkema (1996). We explore this by considering the behavior of an initial condition given by a linear inertia-gravity wave solution to (6)-(9) with $\beta = 0$,

$$\begin{aligned} h &= h_0 + a_0 \sin(kx - \omega t) \\ s &= -\frac{\omega a_0}{k c_0^2} \cos(kx - \omega t) \\ v &= -\frac{\gamma a_0}{k c_0^2} \sin(kx - \omega t) \end{aligned}$$

and $V = 0$. The amplitude is a_0 and $\omega^2 = \gamma^2 + c_0^2 k^2$. While very idealized, this initial condition is representative of a low-mode internal tide radiated from some localized topography. Using the MCC-f model we can follow disintegration of this sinusoidal internal tide into nonhydrostatic nonlinear waves and explore the role of the nonlinear inertia-gravity waves.

An example of the evolution of a linear sinusoidal disturbance with amplitude $a_0 = 0.06$ and wavelength $\lambda = 2.8$ with $h_0 = 0.25$ and $\beta^{1/2} = 0.02$ is shown in Figure 7. The linear internal tide has a frequency $\omega = 1.394$. Nonlinear inertia-gravity waves for these values of h_0 and λ are of the lobate class (c.f. Figure 3b). The interface η is shown over four periods, λ/c_{0f}, of the linear inertia-gravity wave in a frame moving with the linear wave speed c_{0f} (> 0). Also shown in the figure is the evolution of the same initial condition from the hydrostatic ($\beta = 0$) model. The initial sine wave steepens and by $tc_{0f}/\lambda = 1$ the hydrostatic solution

goes to breaking (shock formation). The nonhydrostatic dispersion of the MCC- f solution prevents breaking and gives rise to an undular bore. For longer times the disintegration of the initial wave into short nonlinear waves is inhibited and for $tc_{0f}/\lambda \geq 2.5$ the MCC-f solution consists of a spreading packet of short waves riding on a long, nonlinear tide that is very close to the hydrostatic solution. By the end of the calculation one small solitary-like wave (at $x - c_{0f}t \approx 2.3$) has separated from the packet. The short waves are not phase locked to the long wave and in this example they propagate slower than the long wave. The leading solitary-like wave remains close to the shock in the hydrostatic solution.

Another example for the same parameters except for a larger initial amplitude, $a_0 = 0.1$, is shown in Figure 8. The larger amplitude leads to generation of many more and larger short nonhydrostatic waves. However, the qualitative behavior is the same. The disintegration of the initial condition into short waves is ultimately inhibited, leaving behind a long nonlinear tide underneath the shortwave packet. Again the longwave part of the MCC-f solution is very close to the hydrostatic solution.

Recall that these "short" waves are still dynamically long and only weakly nonhydrostatic. We use the terms short and long to distinguish the relative scales of waves that emerge. The short waves depend fundamentally on the nonhydrostatic dispersion and typically only weakly on the rotation. The long waves are essentially hydrostatic and are strongly controlled by rotation. This dynamical separation is highlighted by examining the transverse shear, v, which may act as a low-pass filter since the short solitary-like waves will typically have a weak expression in v (Gerkema, 1996; Gilman et al., 1996). The v fields for the MCC-f and hydrostatic solutions at $tc_{0f}/\lambda = 4$ of the previous two figures are shown in Figure 9. The hydrostatic and nonhydrostatic solutions are nearly identical for the $a_0 = 0.06$ runs and quite close for the $a_0 = 0.1$ case.

The initiation of breaking in the hydrostatic solutions leads to the continual loss of energy until that solution settles onto a long wave. The total energy (given by (12) with $\beta = 0$, integrated over the wavelength) in the two hydrostatic solutions is shown in Figure 10. By

the end of each run the energy reaches a new equilibrium. This new wave is very close to the "longwave" part of the MCC-f solutions. This is particularly clear for in Figure 7, but also true for the other example.

Also shown in Figures 7 and 8 at $tc_{0f}/\lambda = 4$ are the nonlinear inertia-gravity wave solutions with the same energy and wavelength as in the hydrostatic solution at this point. They are reasonably close to the long wave portion of the MCC-f and hydrostatic solutions, and suggest that the two solutions have settled onto a nonlinear inertia-gravity wave with the short nonhydrostatic waves superimposed. There will be nonlinear interaction between the short and long waves (Gilman et al., 1995, 1996; Helfrich, 2007a), and this may explain the differences between the exact nonlinear solution and the longwave part of the MCC-f and hydrostatic model solutions. Furthermore, at a given wavelength there is a continuum of nonlinear inertia-gravity wave solutions up to the limiting amplitude (c.f. Figure 3b for $\lambda = 2.78$). So it is quite possible that two or more of these solutions have been generated.

By inference, the energy in the short waves in the MCC-f solutions is given approximately by the loss of energy in the hydrostatic solutions. For $a_0 = 0.06$ and 0.1, about 2.6% and 10.2%, respectively, of the initial energy is goes into the short nonhydrostatic waves. The energy loss from the hydrostatic solutions, or conversely, the energy transfer to the short nonhydrostatic nonlinear waves, as a function of amplitude of the initial linear inertia-gravity wave, a_0, for $h_0 = 0.25$ and $\lambda = 2.8$ is summarized in Figure 11. Substantial loss of energy from the initial tide due to breaking (or into short nonhydrostatic waves) does not occur until a threshold amplitude $a_0 \approx 0.04$ is exceeded. Below the threshold, solutions from the hydrostatic model and the MCC-f equations are nearly identical. This threshold is an important result and is the consequence of the low-frequency rotational dispersion. It shows that not all internal tides will steepen and produce short solitary-like waves. Calculations were not continued beyond $a_0 = 0.1$ due to the appearance of finite wavenumber shear instability of both the emerging solitary waves and the long inertia-gravity wave (Jo and Choi, 2002). The degree of numerical filtering required to keep the instability from overwhelming the calculations began to influence the evolution.

Changes in the nonhydrostatic parameter β do not change these basic results as might be expected from stability of the nonlinear inertia-gravity waves to β. However, the properties of short waves produced from the steepening are affected. Figure 6 shows the MCC-f solutions for $\beta^{1/2} = 0.01, 0.02$, and 0.04 with the initial conditions of Figure 7 at $tc_{0f}/\lambda = 4$. The amplitudes of the short waves increase with decreasing β and, as expected from the properties of MCC solitary waves in this amplitude range, the wave width decreases. The underlying long inertia-gravity wave is essentially the same. The high wavenumber wiggles on the $\beta^{1/2} = 0.04$ solution near $x - c_{0f}t = 1.2$ are the beginnings of the Kelvin-Helmholtz shear instability which is enhanced with increasing β.

The examples with $h_0 = 0.25$ and $\lambda = 2.8$ lead to underlying nonlinear inertia-gravity waves that are in the lobate class. Generally, the lobate class waves for a fixed frequency or wavelength exist over a larger range of amplitudes then the corner class waves. Thus, in the corner regime it is more likely that the initial sinusoidal wave may have more energy than the largest possible nonlinear inertia gravity wave. Figures 3b and 4 show that to move into the corner class either ω must be increased (or λ decreased) with h_0 fixed, or h_0 decreased with ω (or λ) fixed. Taking the latter approach and setting $h_0 = 0.1$ and $\lambda = 1.924$ (linear wave frequency $\omega = 1.4$) puts the limiting inertia-gravity wave in the corner class. The limiting wave has $h_m = 0.0862$ and $h_M = 0.1357$ and has total energy per wavelength equal to a linear inertia-gravity wave with amplitude $a_0 = 0.0194$.

Figure 13 shows numerical solutions for a case with $h_0 = 0.1$, $\lambda = 1.924$, and $a_0 = 0.015$. The total energy of the initial wave is within the range of nonlinear inertia-gravity wave solutions. The solutions of both the MCC-f (with $\beta^{1/2} = 0.02$) and hydrostatic models are much the same as the previous examples with production of short solitary-like waves in the MCC-f model inhibited once the solutions settle on underlying long nonlinear wave that is again almost identical to the hydrostatic solution.

The solution becomes quite different when the initial amplitude is increased. An example with $a_0 = 0.025$ is shown in Figure 14. The other parameters are unchanged. The initial

energy is now outside the range of nonlinear inertia-gravity wave solutions. As before, the hydrostatic solution proceeds to breaking and the MCC-f solution develops an undular bore that rapidly separates into a train of solitary-like waves. As the evolution progresses, the breaking in the hydrostatic model diminishes until the solution settles on a nonlinear inertia-gravity wave with total energy just slightly less than that of the maximum inertia-gravity wave with this wavelength. The hydrostatic solution at $tc_{0f}/\lambda = 4$ is very close to this theoretical, limiting solution as shown in Figure 14.

The MCC-f solution, on the other hand, continues to disintegrate until it consists primarily of individual solitary waves. There is little indication from the η solution of an underlying inertia-gravity wave similar to the hydrostatic solution. Thus the rotational dispersion did not arrest the disintegration of the initial tide. One difference between this case and the others is the large amplitude of the emerging solitary waves. At $tc_{0f}/\lambda = 2.5$ the largest wave has an amplitude $\eta_0 \approx -0.16$. Thus $|\eta_0|/h_0 \approx 1.6$, compared to $|\eta_0|/h_0 \approx 0.4$ in Figure 8. With such large waves a significant fraction of the initial mass of the upper layer ($= h_0\lambda$) is contained in the solitary waves. In the hydrostatic solution, all the mass remains in the long wave part of the solution.

The transverse vertical shear v for the MCC-f and hydrostatic runs in Figure 14 at the last time shown are plotted in Figure 15. The hydrostatic solution is comparable to those shown in Figure 9. The MCC-f solution is quite different. It is characterized by a large jump in v at the location of the largest solitary wave. The magnitude of v is the same order as the hydrostatic solution. Thus the v field, that in the previous examples effectively filtered out the short waves to show clearly the underlying inertia-gravity wave, is now affected by the short solitary wave(s). Indeed, a jump in v is precisely what is predicted by weakly nonlinear theories for the radiation damping of a solitary wave in a rotating system (Grimshaw et al., 1998a). This implies a strong, continuing interaction between the solitary waves, or at least with the largest one, with the inertia-gravity waves. The longwave component of the MCC-f solution is the result of the solitary wave(s) rather than an underlying long wave that remains after the disintegration. When the nonhydrostatic calculation is carried further the large

solitary wave decays and there is some evidence of the emergence of a quasi-periodic wave packet as found in Helfrich (2007a). However, the large amplitudes of the waves and the periodic domain make this difficult to identify unambiguously. It does show that the transfer of energy from the long, hydrostatic part of the solution to the short nonhydrostatic waves can be, in part, reversed.

This last example shows that the energy loss in the hydrostatic model will not always provide a good estimate of the energy transfered to the short nonhydrostatic waves. The hydrostatic model does, however, give an approximate lower bound on the energy transfer. The energy per wavelength of the hydrostatic solution as a function of time for the two $h_0 = 0.1$ calculations above are shown in Figure 10. The energy lost from the hydrostatic solution as a function of the initial amplitude a_0 is given in Figure 16 for a series of runs with the same parameters, $h_0 = 0.1$ and $\lambda = 1.924$. As before, there is a threshold amplitude, now about 0.01, below which the rotational dispersion prevents breaking in the hydrostatic calculation. Also shown in the figure by the solid line is the energy of the initial condition in excess of the energy of the largest, limiting nonlinear inertia-gravity wave solution for these parameters. Energy loss above this curve for $a_0 > 0.0194$ implies that the final state has less energy than the limiting wave, and vice versa. MCC-f runs with initial amplitudes $a_0 \lesssim 0.18$ behave as shown in Figure 13, with the disintegration arrested by rotational dispersion and longwave part of the solution close to the hydrostatic case. Then energy transfered into the short waves is approximately the same as lost from the hydrostatic solution. When $a_0 \gtrsim 0.2$ the MCC-f solutions behave as shown in Figure 14, suggesting that most of the energy goes into the shorter solitary-like waves. The transition in behavior occurs at $a_0 = 0.0194$ where the initial wave has more energy than the limiting nonlinear inertial-gravity wave. Calculations with $\beta^{1/2} = 0.01$ yield the same results, though the solitary wave properties are modified.

Nearly complete disintegration of the initial internal tide does, for the examples in Figures 13 and 14, require an initial energy greater than the energy of the limiting nonlinear inertia-gravity wave. Whether this is always the case, or depends upon the particular parameters or the shape of the initial condition (e.g. departure from sinusoidal shape and proximity to

a nonlinear inertia-gravity wave), will require more study. However, some calculations have been made for $h_0 = 0.25$ and $\lambda = 1.571$ ($\omega \approx 2$) that put the limiting wave in the corner class. A calculation with $a_0 = 0.05$, shown in Figure 17, has an initial energy well in excess of the limiting wave. The disintegration is not as complete as the earlier example. The longwave part of both the η and v fields are close to the hydrostatic solution. The largest solitary wave does cause the transverse velocity v to depart from the hydrostatic solution in the same sense as Figure 15. One distinction between these two examples is the nonlinearity of the solitary waves. In Figure 14 $|\eta_0|/h_0 \approx 1.8$, and $|\eta_0|/h_0 \approx 0.7$ in Figure 17. Increasing nonlinearity of the solitary waves leads to a stronger interaction between the short and long waves. This apparently prevents the solution from settling into a state in which a packet of short waves is essentially superimposed on a stable, long inertia-gravity wave.

4. Discussion

The fully nonlinear MCC-f model [(6)-(9)] solutions show that the nonlinear inertial-gravity waves prevent the total disintegration of the initial internal tide, consistent with earlier studies of weakly-nonlinear waves. However, the conditions for the disintegration of the initial internal tide into short solitary waves are further clarified. For the small, oceanographically reasonable values of the nonhydrostatic parameter $\beta^{1/2} = H/L_R$ considered, there is a minimum amplitude of the initial tide below which the rotational dispersion is sufficient to prevent nonlinear steepening and breaking. It is, however, well below the limiting amplitude for the nonlinear inertia-gravity waves. The initiation of breaking and energy loss in the hydrostatic model runs (Figures 11 and 16) begins for $a_0/h_0 \approx 0.12 - 0.16$, though it is not clear from these two choices of h_0 and λ that this will always be the case. The degree of disintegration increases monotonically above this threshold, but is still incomplete. A growing fraction of the energy in the initial tide is shed into short solitary waves, leaving a long nonlinear tide on which packets of shorter waves propagate. The properties of the underlying nonlinear tide are well approximated by solutions of the hydrostatic (shallow water) limit of the governing equations. Initial internal tide energies above the energy of the limiting nonlinear inertia-gravity

wave may lead to a complete disintegration of the internal tide into shorter solitary waves, though the nonlinearity of the short waves and their interaction with the inertia-gravity waves appears to be an important aspect of this process. In these cases the hydrostatic model does not give an accurate representation of the longwave part of the solution. Conditions which give underlying lobate-class inertia-gravity waves are less likely undergo significant disintegration since these waves exist over a larger range of amplitudes than the corner-class waves.

Numerical calculations (not shown) with weakly nonlinear versions of the equations (essentially those used by Gerkema (1996)) give similar results. However, the weakly-nonlinear models can result in substantial quantitative differences for even moderate amplitudes. This is due largely to the differences in the hydrostatic, nonlinear inertia-gravity waves in each system. For example, the Boussinesq set of equations from Gerkema and the related unidirectional propagation, rotating KdV equation (Ostrovsky, 1978) have only the corner-class inertia-gravity waves in the hydrostatic limit. The addition of cubic nonlinearity to the rotating KdV model gives rise to the lobate class hydrostatic wave, but eliminates the corner class. In addition to expanding the applicability of the model for the short solitary-like waves to larger amplitudes, the MCC-f equations the advantage of more accurate representation of the important long nonlinear tides. A cost of using these equations is the presence of Kelvin-Helmholtz instability at very short scales that can overwhelm the numerical solutions. This can, however, be eliminated by retaining only the $O(\beta)$ terms in the dispersion operator $D_2 - D_1$ in (2) (see discussion following (4)). This truncation causes minor changes in the solitary wave properties and results in equations that are close to those obtained when cubic nonlinear effects are included in the Gerkema (1996) model. The truncation leaves the long, hydrostatic waves unaffected and has been shown to give good results for the radiation damping of solitary waves when compared to the full MCC-f equations (Helfrich, 2007a).

This MCC-f model is limited to two-layers, though extension to multiple layers is possible. However, the system of governing equations grows and rapidly becomes very cumbersome. It is probably easier and more accurate to use a continuously stratified, nonhydrostatic numerical model such as in Lamb (1994). The role of the nonlinear inertia-gravity waves should be qual-

itatively unchanged since these wave solutions persist with similar properties for continuous stratifications (Helfrich, 2007b)

The model results can be applied to recent observations of large amplitude internal waves in the South China Sea. Ramp et al. (2005) has shown that very large solitary waves with amplitudes greater than 100 m can be found in the western part of the South China Sea. From an analysis of the arrival of the packets of solitary waves Ramp et al. (2005) and Zhao and Alford (2006) have determined that the waves were generated by tidal flow over the abrupt topography about 400 km to the east in the Luzon Strait near the Batan Islands. Satellite observations of the area indicate that the solitary waves first appear about 100 km west of the strait (Zhao et al., 2004), pointing to the emergence of the solitary waves from the radiating internal tide west of the strait (c.f. Lien et al., 2005). The tidal currents in generation region are mixed, with both the primary semidiurnal and diurnal constituents of comparable magnitude (Ramp et al., 2005; Zhao and Alford, 2006). At this latitude, 21° N, the diurnal frequency is $1.4f$ and the semidiurnal frequency is $2.7f$. An estimate of h_0 can be found from the continuously stratified longwave eigenmode solution using density profile in the mid-basin (from D. Farmer). The lowest eigenmode has a linear, non-rotating longwave phase speed $c_0 = 2.85$ m s^{-1} and the zero-crossing of the horizontal velocity about 600 m deep in 3000 m of water. Thus $h_0 \approx 0.2$ in the two-layer approximation. For these tidal frequencies and this stratification, the semidiurnal internal tide is in the corner class and the diurnal tide is in the lobate class (c.f. Figures 3b and 4). The latter will have nonlinear tide solutions over a large range of amplitudes (limiting wave at $(h_m, h_M) = (0.125, 0.493)$). The semidiurnal nonlinear internal tide solutions will exist only over a limited range of amplitudes (limiting wave at $(h_m, h_M) = (0.1926, 0.2159)$).

As a test that the model results are relevant, a simple application to the South China Sea conditions has been made. The longwave phase speed $c_0 = 2.85$ m s^{-1} from the density profile gives $g' = 0.017$ m s^{-2} for a two-layer model with $h_0 = 0.2$ and $H = 3000$ m. At 21° N, the deformation radius $L_R = \sqrt{g'H}/f = 137$ km. The linear diurnal and semidiurnal internal tides have nondimensional (by L_R) wavelengths $\lambda = 2.56$ and 1.0, respectively. Figure 18 shows

two runs with the MCC-f model for these wavelengths with initial amplitudes $a_0 = 0.0167$, or 50 m in dimensional units. The calculations were made with $\beta^{1/2} = 3/137 \approx 0.02$. The diurnal tide (Figure 18a) is shown at $t = 6.17$ and the semidiurnal tide (Figure 18b) at $t = 8.14$. These nondimensional times correspond to propagation at the respective linear phase speeds c_{0f} of about 480 km, the distance from the Luzon Strait to the western side of the basin. As expected, the diurnal tide has remained intact, while semidiurnal tide has begun to disintegrate, producing a lead solitary wave with amplitude $\eta_0 \approx 0.05$, or 150 m.

From these nonhydrostatic modeling results we expect that the internal tide (of a given amplitude) will remain largely intact at the diurnal frequency and experience significant disintegration into short solitary waves at the semidiurnal frequency. This is indeed what is observed. Figures 8 and 9 in Zhao and Alford (2006) show that the arrival of large internal solitary waves at the western side of the basin occurs when the generating tides have maximum western velocity at Luzon (after taking into account a phase shift consistent with propagation times across the basin) and are dominantly semidiurnal in character. When the tides in Luzon change to dominantly diurnal, the large solitary waves are eliminated. This happens even though the magnitude of the barotropic flow in the strait is comparable in both regimes. Furthermore, Zhao and Alford (2006) (see their Figure 2) find that the amplitude of the low-pass filtered internal tide at the western slope mooring is smaller by a factor of about two during the semidiurnal regime than during the diurnal phase. This is in rough agreement with Figure 18. New measurements by D. Farmer from moorings in the mid-basin, about 200 km west of the generation site show a the same relation between the dominant frequency of the Luzon barotropic tide and the occurrence of large solitary waves at the moorings (D. Farmer and C. Jackson, pers. comm.).

This simple comparison with the observational data qualitatively supports the theoretical and modeling conclusions, though more extensive and direct comparisons with the data are needed. This should include modeling of the generation of the radiated internal tide since that sets the initial condition for the disintegration. It will probably be necessary to also

incorporate variations in topography along the propagation path that influence the evolution of both the internal tide and any solitary waves produced by the disintegration.

Acknowledgments: This work was supported by a Woods Hole Oceanographic Institution Mellon Independent Study Award and ONR Grant N000140610798. The authors thank David Farmer and Chris Jackson for discussion of their data.

References

Camassa, R., Choi, W., Michallet, H., Rusås, P.-O., and Sveen, J., 2006: On the realm of validity of strongly nonlinear asymptotic approximations for internal waves. *J. Fluid Mech.*, **549**, 1–23.

Choi, W., and Camassa, R., 1999: Fully nonlinear internal waves in a two-fluid system. *J. Fluid Mech.*, **396**, 1–36.

Gerkema, T., 1996: A unified model for the generation and fission of internal tides in a rotating ocean. *J. Mar. Res.*, **54**, 421–450.

Gerkema, T., 2001: Internal and interfacial tidal tides: beam scattering and local generation of solitary waves. *J. Mar. Res.*, **59**, 227–255.

Gerkema, T., and Zimmerman, J. T. F., 1995: Generation of nonlinear internal tides and solitary waves. *J. Phys. Oceano.*, **25**, 1081–1095.

Gilman, O. A., Grimshaw, R., and Stepanyants, Y. A., 1995: Approximate analytical and numerical solutions of the stationary ostrovsky equation. *Stud. Appl. Math.*, **95**, 115–126.

Gilman, O. A., Grimshaw, R., and Stepanyants, Y. A., 1996: Dynamics of internal solitary waves in a rotating fluid. *Dyn. Atmos. Oceans*, **23**, 403–411.

Grimshaw, R., He, J.-M., and Ostrovsky, L., 1998a: Terminal damping of a solitary wave due to radiation in rotational systems. *Stud. Appl. Math*, **101**, 197–210.

Grimshaw, R., Ostrovsky, L., Shrira, V. I., and Stepanyants, Y. A., 1998b: Long nonlinear surface and internal gravity waves in a rotating ocean. *Surveys in Geophys.*, **19**, 289–338.

Grimshaw, R. H. J., and Smyth, N., 1986: Resonant flow of a stratified fluid over topography. *J. Fluid Mech.*, **169**, 429–64.

Hammack, J. L., and Segur, H., 1978: Modelling criteria for long water waves. *J. Fluid Mech.*, **84**, 359–373.

Helfrich, K. R., 2007a: Decay and return of internal solitary waves with rotation. *Phys. Fluids.*, **19**, 026601.

Helfrich, K. R., 2007b: Models for continuosly stratified nonlinear low-mode internal tides. *J. Phys. Oceano.*, in prep.

Helfrich, K. R., and Melville, W. K., 2006: Long nonlinear internal waves. *Ann. Rev. Fluid Mech.*, **38**, 395–425.

Holloway, P. E., Pelonovsky, E., and Talipova, T., 1999: A generalized korteweg-de vries model of internal tide transformation in the coastal zone. *J. Geophys. Res.*, **104**, 18333–18350.

Jiang, and Tadmor, 1998: Nonoscillatory central schemes for multidimensional hyperbolic conservation laws. *SIAM J. Sci. Comp.*, **19**, 1892–1917.

Jo, T.-C., and Choi, W., 2002: Dynamics of strongly nonlinear internal solitary waves in shallow water. *Stud. Appl. Math.*, **109**, 205–227.

Kakutani, T., and Yamasaki, N., 1978: Solitary waves on a two-layer fluid. *J. Phys. Soc. Japan*, **45**, 674–679.

Lamb, K., 1994: Numerical experiments on internal wave generation by strong tidal flow across afinite amplitude bank edge. *J. Geophys. Res.*, **99**, 843–864.

Lee, C.-Y., and Beardsley, R. C., 1974: The generation of long nonlinear internal waves in a weakly stratified shear flow. *J. Geophys. Res.*, **79**, 453–462.

Leonov, A. I., 1981: The effect of the earth's rotation on the propagation of weak nonlinear surface and internal long oceanic waves. *Annals NY Acad. Sci.*, **373**, 150–159.

Lien, R.-C., Tang, T. Y., Chang, M. H., and DAsaro, E. A., 2005: Energy of nonlinear internal waves in the south china sea. *Geophys. Res. Lett.*, **32**, L05615, doi:10.1029/2004GL022012.

Maxworthy, T., 1979: A note on the internal solitary waves produced by tidal flow over a three-dimensional ridge. *J. Geophys. Res.*, **84**, 338–46.

Melville, W. K., and Helfrich, K., 1987: Transcritical two-layer flow over topography. *J. Fluid Mech.*, **178**, 31–52.

Melville, W. K., Tomasson, G. G., and Renouard, D. P., 1989: On the stability of kelvin waves. *J. Fluid Mech.*, **206**, 1–23.

Michallet, H., and Barthelemy, E., 1998: Experimental study of interfacial solitary waves. *J. Fluid Mech.*, **366**, 159–77.

Miyata, M., 1985: Long internal waves of large amplitude. *La Mer*, **23**, 43–48.

Miyata, M., 1987: Long internal waves of large amplitude. K. Horikawa, and H. Maruo, Eds., *Nonlinear Water Waves*, IUTAM, Springer-Verlag, 399–406.

New, A. L., and Estaban, M., 1999: A new korteweg-de vries-type theory for internal solitary waves in a rotating continuously-stratified ocean. E. N. Pelinovsky, and V. I. Talanov, Eds., *Ocean Subsurface Layer: Physical Processes and Remote Sensing*, Nizhny Novgorod (Russia): Applied Physics Institute Press, 173–203.

Ostrovsky, L., 1978: Nonlinear internal waves in a rotating ocean. *Oceanology*, **18**, 119–1125.

Ostrovsky, L., and Grue, J., 2003: Evolution equations for strongly nonlinear internal waves. *Phys. Fluids*, **15**, 2934–2948.

Plougonven, R., and Zeitlin, V., 2003: On periodic inertia-gravity waves of finite amplitude propagating without change of form at sharp density-gradient interfaces in the rotating fluid. *Phys. Lett. A.*, **314**, 140–149.

Ramp, S. R., Tang, T. Y., Duda, T. F., Lynch, J. F., Liu, A. K., Chiu, C.-S., Bahr, F. L., Kim, H.-R., and Y.-J.Yang, 2005: Internal solitons in the northeastern south china sea part i: sources and deep water propagation. *IEEE J. Oceanic Engr.*, **29**, 1157–1181.

Shrira, V. I., 1986: On long strongly nonlinear waves in a rotating ocean. *Izvestiya Atm. Oceanic Phys.*, **22**, 298–305.

Stanton, T. P., and Ostrovsky, L. A., 1998: Observations of highly nonlinear solitons over the continental shelf. *Geophys. Res. Lett.*, **25**, 2695–2698.

Wei, G., Kirby, J. T., Grilli, S. T., and Subramanya, R., 1995: A fully nonlinear boussinesq model for surface waves. part 1. highly nonlinear unsteady waves. *J. Fluid Mech.*, **294**, 71–92.

Zhao, Z., and Alford, M., 2006: Source and propagation of internal solitary waves in the northeastern south china sea. *j. Geophys. Res.*, **111**, C11012, doi:10.1029/2006JC003644.

Zhao, Z., V. Klemas, Q. Z., and Yan, X.-H., 2004: Remote sensing evidence for baroclinic tide origin of internal solitary waves in the northeastern south china sea. *Geophys. Res. Lett.*, **31**, L06302, doi:10.1029/2003GL019077.

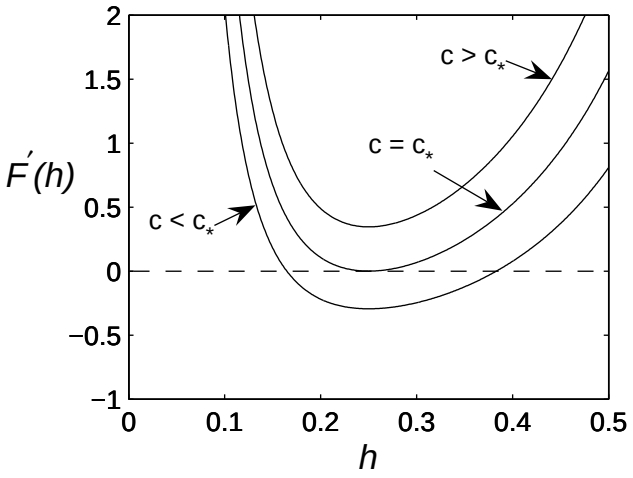

Figure 1: An example of $F'(h)$ from (24) for $h_0 = 0.1$. Zeros of $F'(h)$ occur for $c \leq c_* = 0.625$.

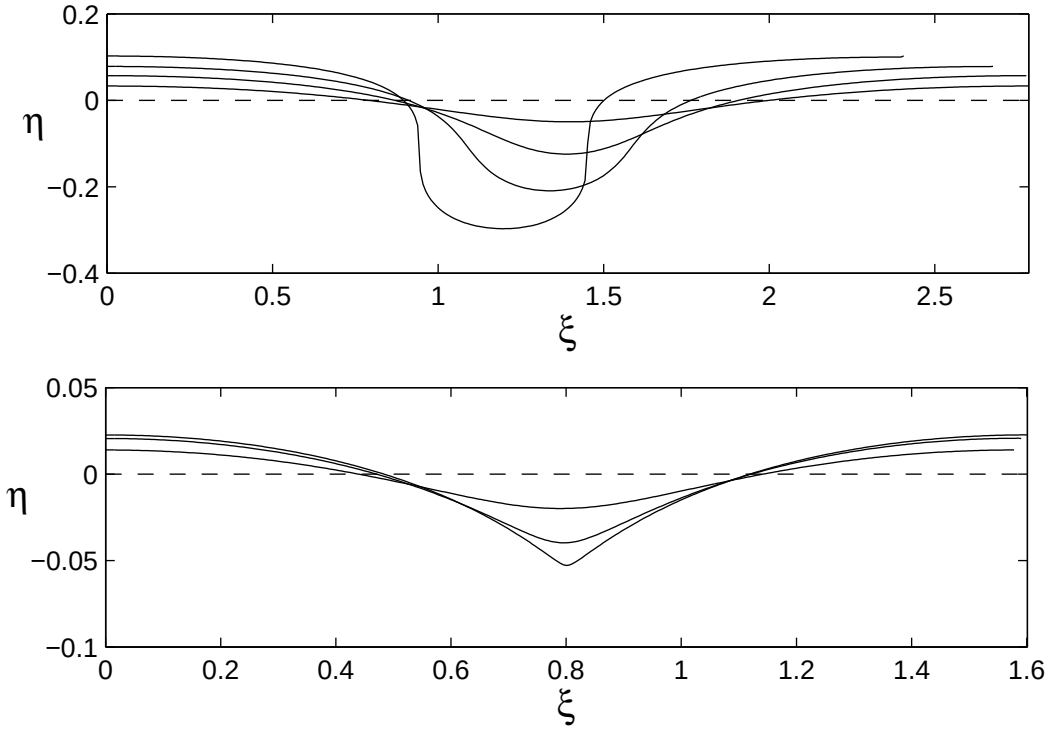

Figure 2: Examples of the two classes of nonlinear inertia-gravity waves for $h_0 = 0.2$. The interfacial displacement $\eta = h_0 - h$ is shown over one wavelength. a) Lobate-class waves for $\omega = 1.4$ and $h_M = 0.3, 0.375, 0.46,$ and 0.55. b) Corner-class waves for $\omega = 2$ and $h_M = 0.27, 0.29,$ and 0.306.

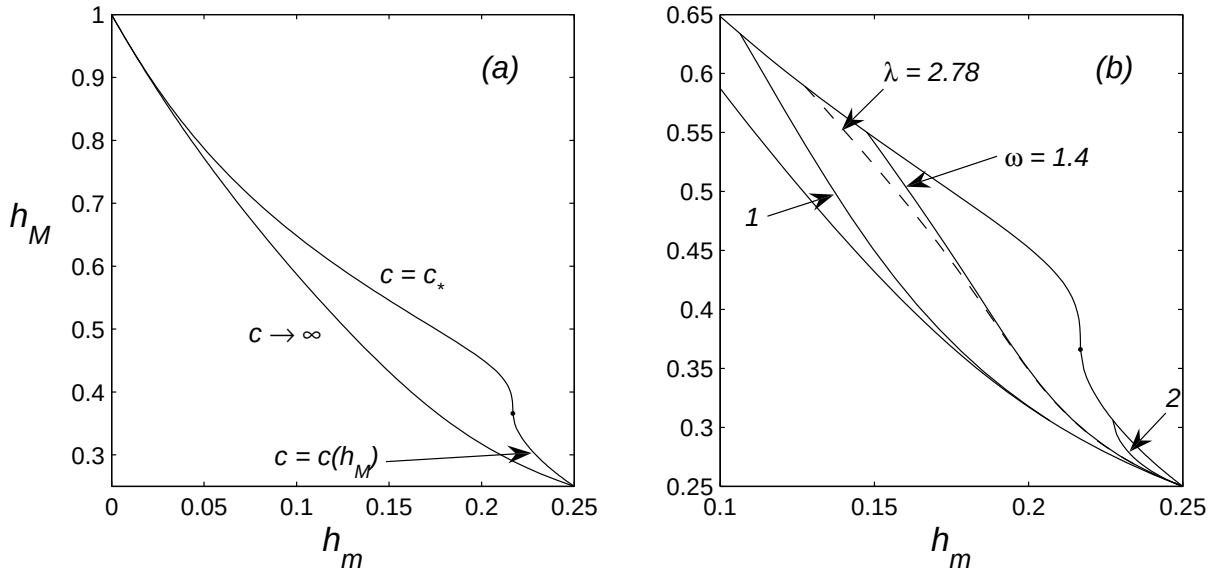

Figure 3: a) Periodic nonlinear inertia-gravity wave solutions for $h_0 = 0.25$ are found everywhere within the region in the h_m- h_M plane bounded by the labeled curves. The small dot indicates the transition point between limiting amplitude corner-class waves to lobate-class waves. b) A close-up showing the loci of nonlinear solutions with frequencies $\omega = 1, 1.4$, and 2, and wavelength $\lambda = 2.78$.

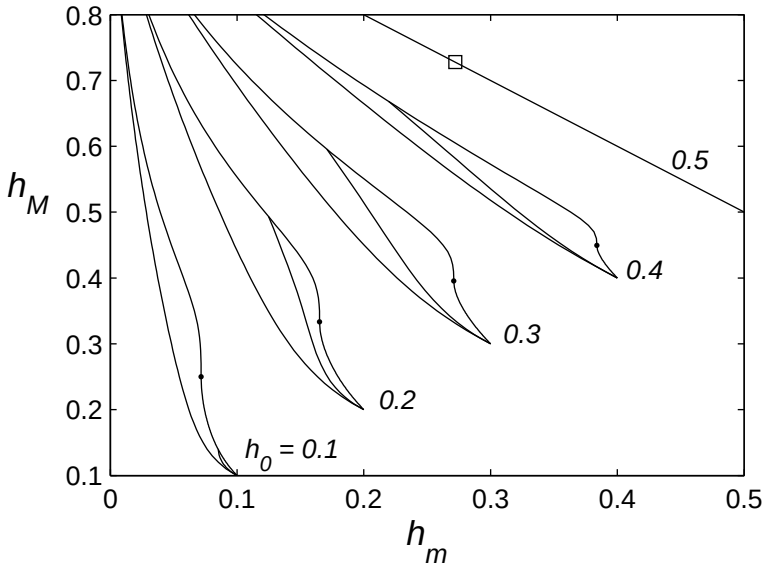

Figure 4: The regions of nonlinear wave solutions for h_0 as indicated. The solid line within each solution domain shows the loci of solutions with $\omega = 1.4$. When $h_0 = 0.5$, the $\omega = 1.4$ solutions extend up to the square.

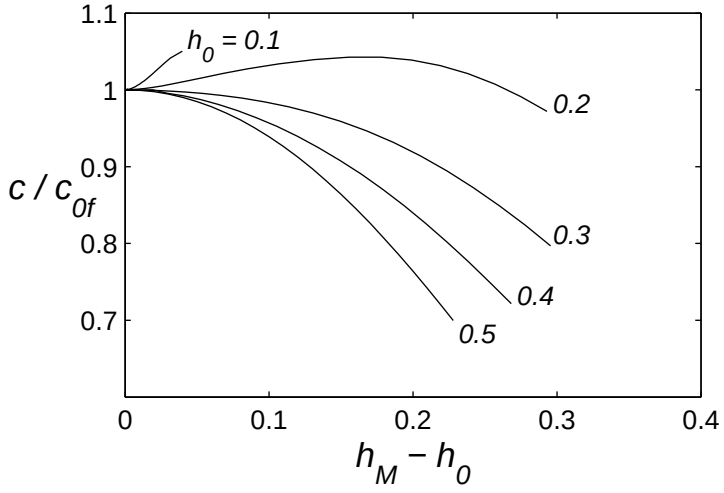

Figure 5: The phase speed c of the $\omega = 1.4$ nonlinear inertia-gravity wave solutions in Figure 4 as a function of wave amplitude, $h_M - h_0$. The speed has been scaled by the linear inertia-gravity phase speed c_{0f}.

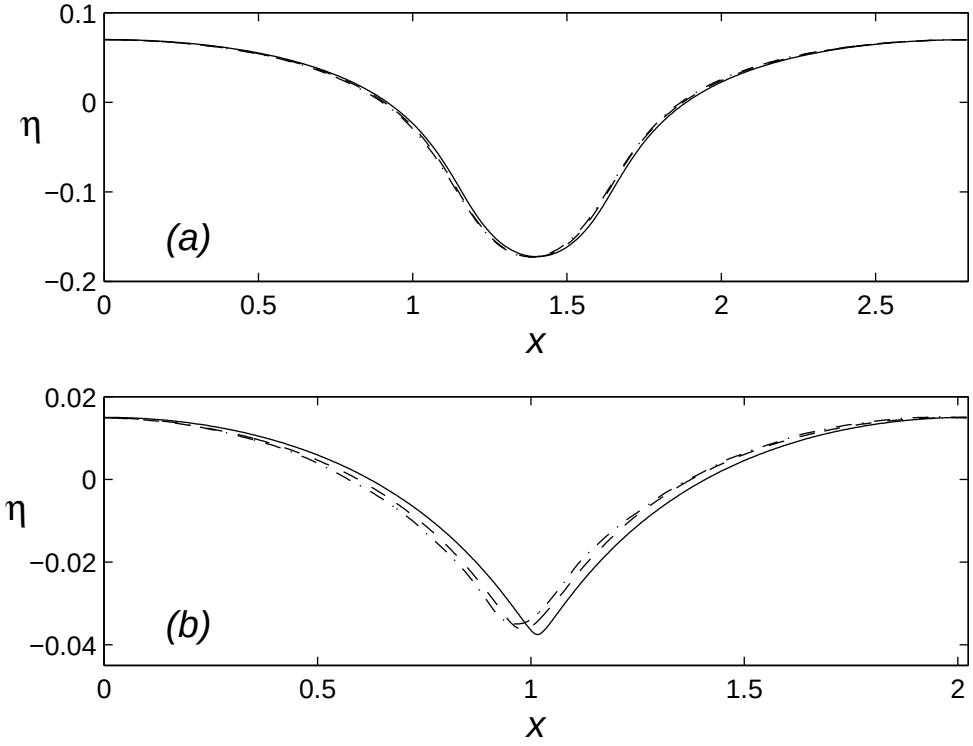

Figure 6: Numerical solutions to the MCC-f equations showing the stability of an initial nonlinear inertia-gravity wave solution to weak nonhydrostatic effects. The solid line shows the initial wave interface displacement η over one wavelength. The solutions with $\beta^{1/2} = 0.02$ (dashed) and 0.04 (dash-dot) are shown after eight periods of propagation. a) Initial lobate-class wave with $h_0 = 0.25$, $\lambda = 2.8$, $h_m = 0.18$, and $h_M = 0.4229$. b) Initial corner-class wave with $h_0 = 0.1$, $\lambda = 2.024$, $h_m = 0.085$, and $h_M = 0.139$.

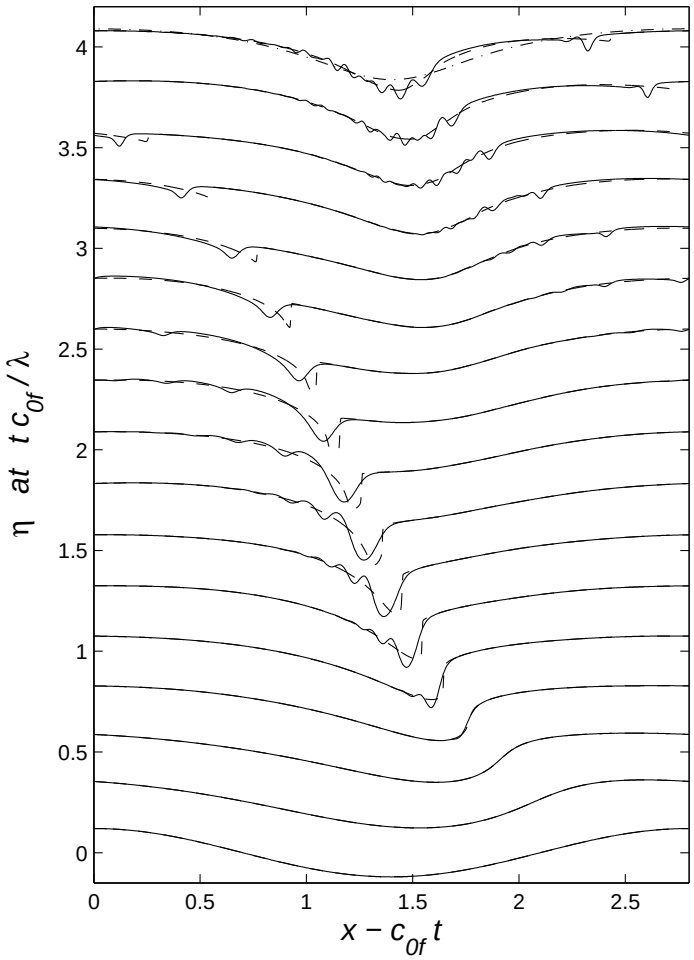

Figure 7: The evolution of an initial linear inertia-gravity wave for $h_0 = 0.25$, $\lambda = 2.8$ and $a_0 = 0.06$. The interfacial displacement η is shown over four periods of the linear wave in a frame moving at the linear phase speed c_{0f}. The MCC-f solution for $\beta^{1/2} = 0.02$ is given by the solid line and the hydrostatic solution by the dashed line. The dash-dot line at $tc_{0f}/\lambda = 4$ is the theoretical nonlinear inertia-gravity wave solution with the wavelength and energy of the hydrostatic solution at that time.

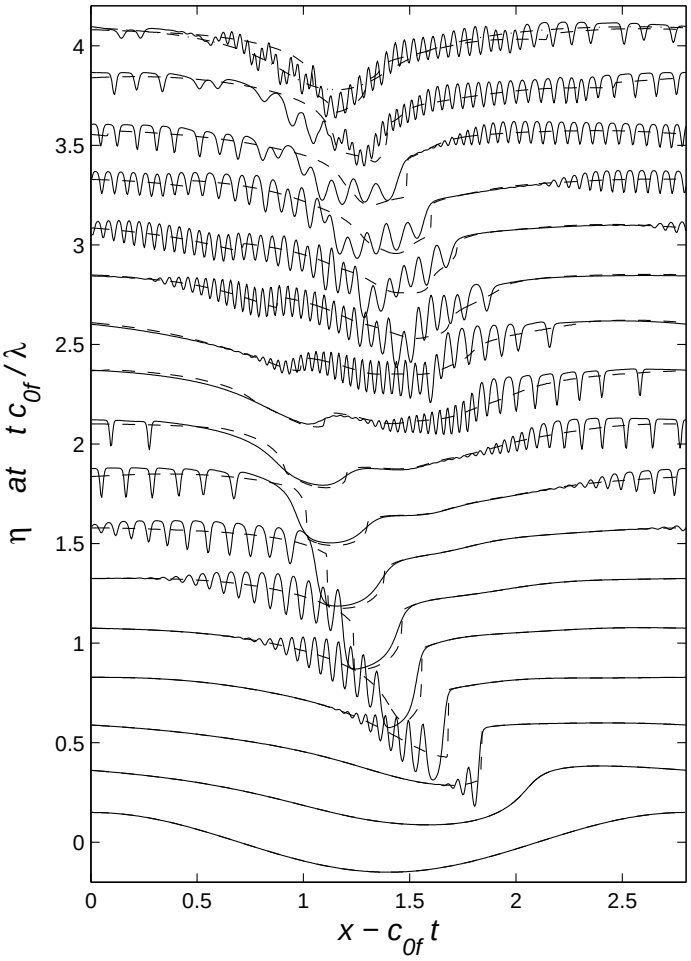

Figure 8: The same as Figure 7 except $a_0 = 0.1$.

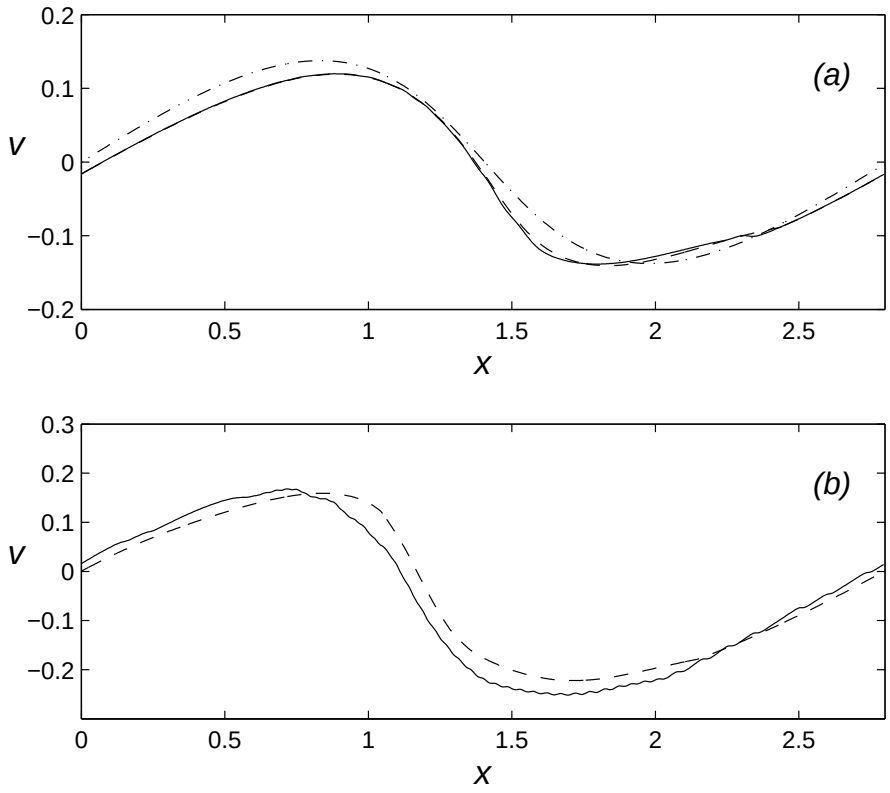

Figure 9: The transverse vertical shear v of the MCC-f (solid) and hydrostatic (dashed) solutions at $t = 4\lambda/c_{0f}$ from a) Figure 7; b) Figure 8. The dash-dot line in (a) is the theoretical nonlinear inertia-gravity wave solution with the wavelength and energy of the hydrostatic solution at this time.

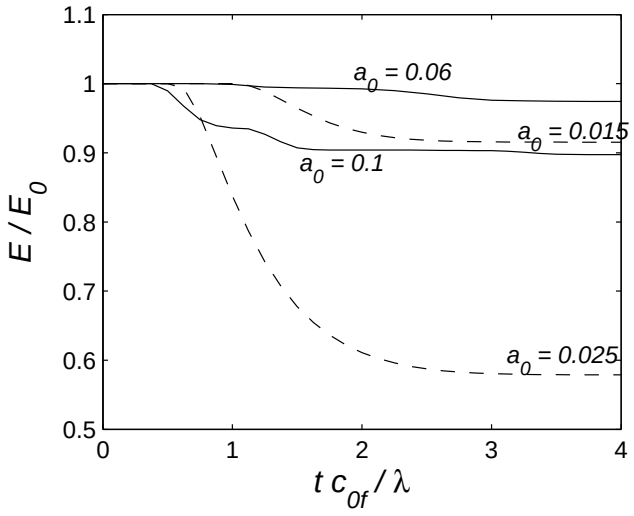

Figure 10: The energy per wavelength, E, of the hydrostatic solutions in Figures 7 and 8 are shown by the solid lines. The initial amplitude a_0 is indicated and the energy is scaled by the initial energy E_0. The results from Figures 13 and 14 are shown by the dashed lines.

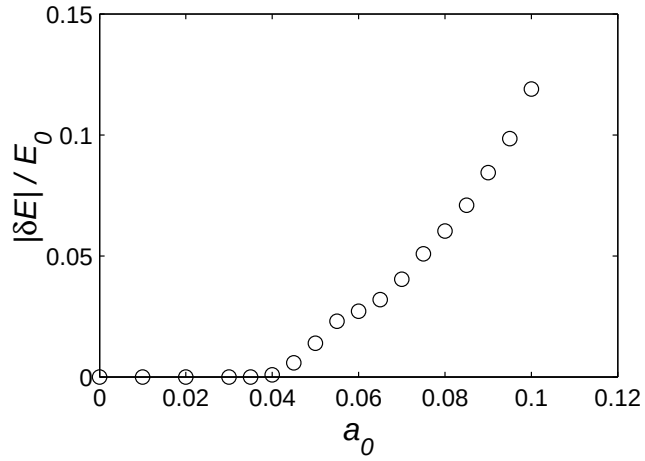

Figure 11: The energy per wavelength lost from the hydrostatic solution $\delta E = E_{end} - E_0$ versus the amplitude a_0 of the initial sinusoidal wave for $h_0 = 0.25$ and $\lambda = 2.8$. E_{end} is the final energy once breaking has stopped.

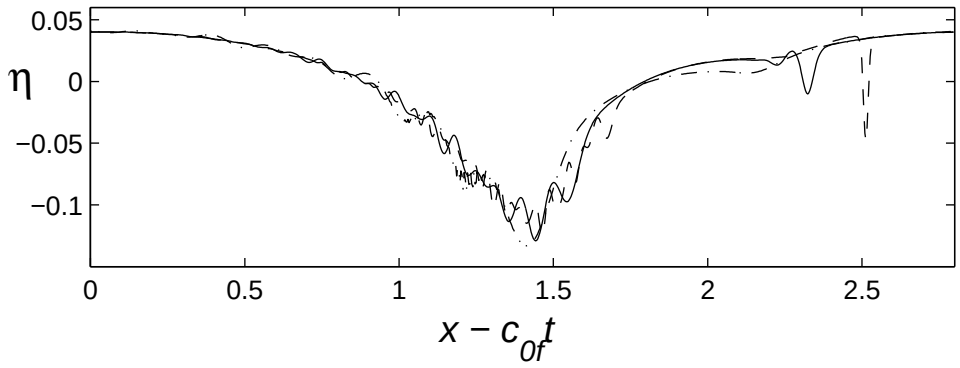

Figure 12: The MCC-f solutions at $t = 4\lambda/c_{0f}$ for $h_0 = 0.25$, $\lambda = 2.8$, $a_0 = 0.06$, and $\beta^{1/2} = 0.1$ (dashed), 0.02 (solid), and 0.04 (dash-dot).

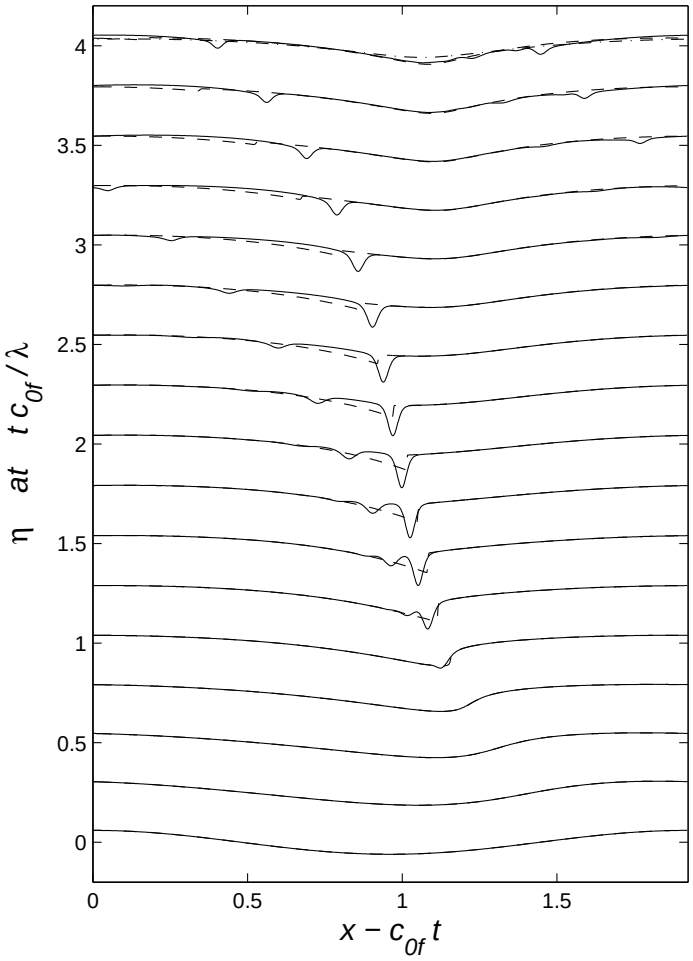

Figure 13: The same as Figure 7 except $h_0 = 0.1$, $\lambda = 1.924$, and $a_0 = 0.015$.

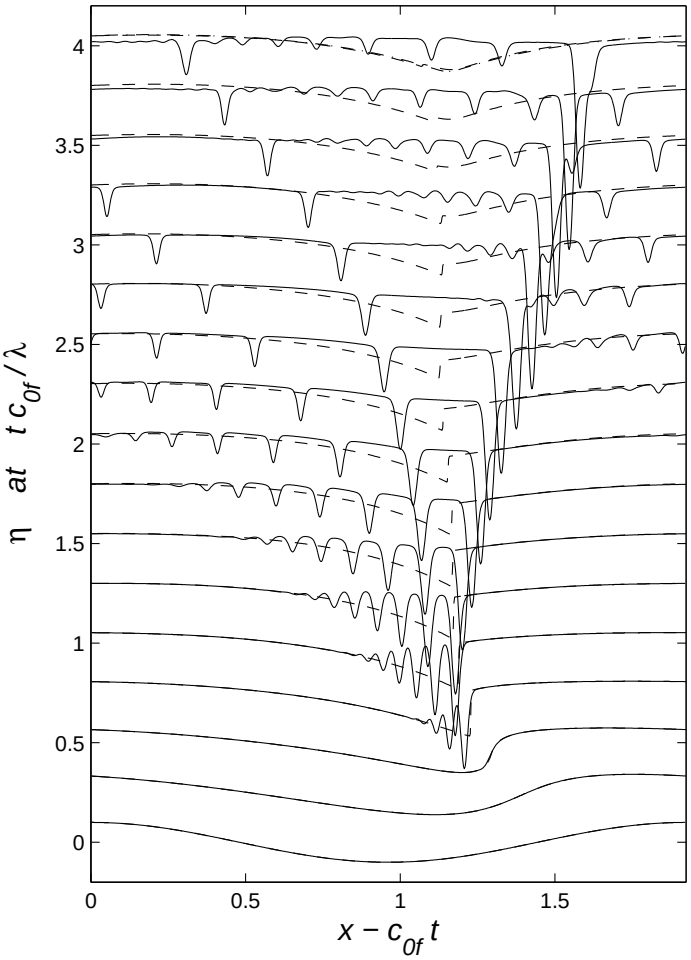

Figure 14: The same as Figure 7 except $h_0 = 0.1$, $\lambda = 1.924$, and $a_0 = 0.025$.

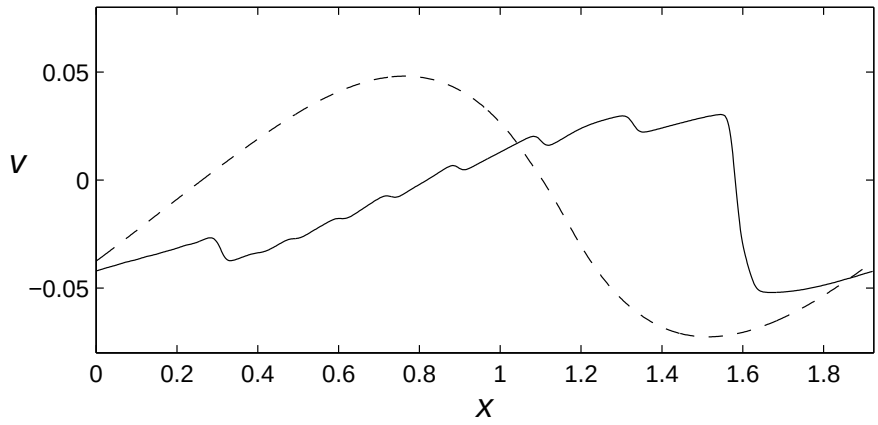

Figure 15: The transverse vertical shear v of the MCC-f (solid) and hydrostatic (dashed) at $t = 4\lambda/c_{0f}$ solutions in Figure 14 .

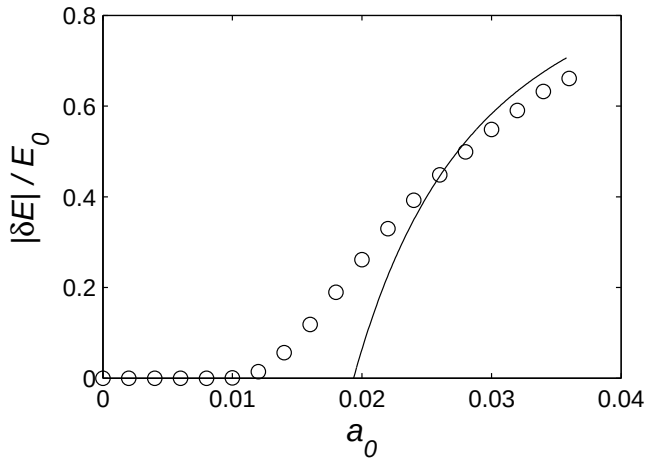

Figure 16: The energy per wavelength lost from the hydrostatic solution $\delta E = E_{end} - E_0$ (circles) versus the amplitude a_0 of the initial sinusoidal wave for $h_0 = 0.1$ and $\lambda = 1.924$. E_{end} is the final energy once breaking has ceased. The solid line is the energy in the initial condition in excess of the limiting nonlinear inertia-gravity wave.

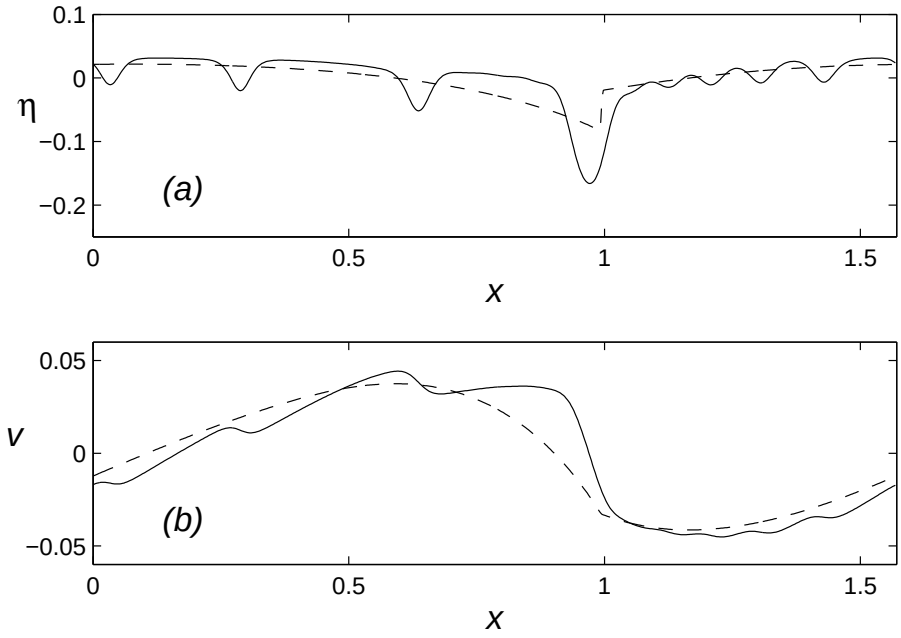

Figure 17: The interface η (a) and the transverse vertical shear v (b) at $t = 4c_{0f}/\lambda$ for an initial linear inertia-gravity wave for $h_0 = 0.2$, $\lambda = 1.57$ and $a_0 = 0.05$. The MCC-f solution with $\beta^{1/2} = 0.02$ is shown by the solid line and the hydrostatic solution by the dashed line.

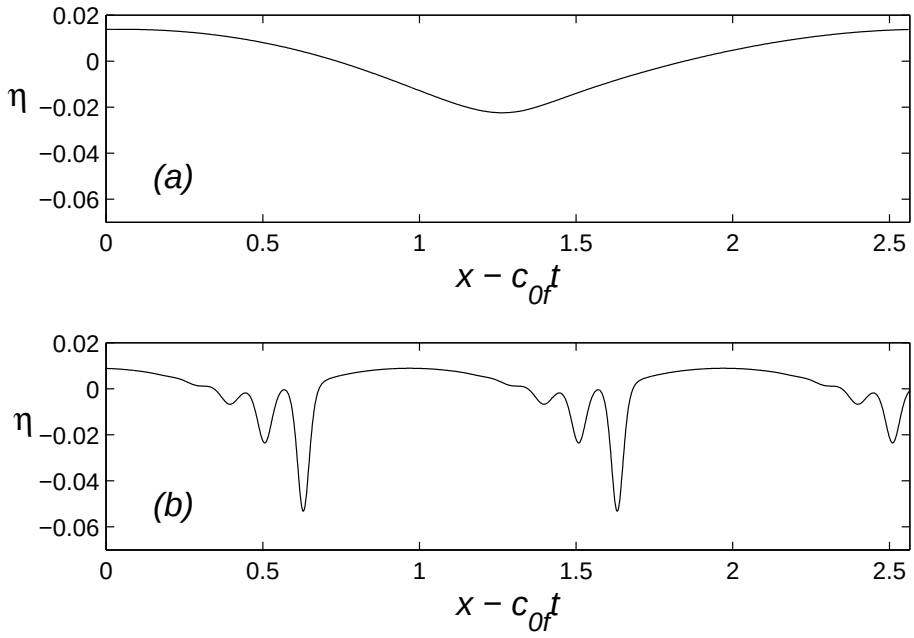

Figure 18: Results from the nonhydrostatic model with conditions approximating the (a) diurnal and (b) semidiurnal tides in the South China Sea. The panels show the interface η at times equal to the time for the linear tides to propagate across the basin. See the text for details. Note that the semidiurnal solution in (b) has been extended in x to a distance equal to the wavelength of the diurnal tide.